




# Composite Carbon-lignin/ Zinc Oxide Nanocrystalline Ball-like Hexagonal Mediated from *Jatropha curcas* L Leaf as Photocatalyst for Industrial Dye Degradation

Bahrul Ulum<sup>1,2</sup> · Sultan Ilyas<sup>2</sup> · Ahmad Nurul Fahri<sup>2</sup> · Inayatul Mutmainna<sup>2</sup> · Muhammad Angga Anugrah<sup>2</sup> · Nurfina Yudasari<sup>3</sup> · Eymal B. Demmalino<sup>1</sup> · Dahlang Tahir<sup>2</sup> 

Received: 10 April 2020 / Accepted: 16 June 2020  
© Springer Science+Business Media, LLC, part of Springer Nature 2020

## Abstract

Composite carbon-lignin/ZnO nanocrystalline has been successfully synthesized mediated by using natural material from castor leaf (*Jatropha curcas* L). The prepared composites were characterized by using Fourier transform infra-red (FTIR), powder X-ray diffraction (PXRD), ultraviolet-visible (UV-Vis) spectroscopy, and scanning electron microscopy (SEM). The crystallite size decreased with increasing the pH due to the atomic crystal in the lattice more stable and also increases with increasing the calcination temperature as the effect of solidification to form carbon-lignin/ZnO. The bandgap strongly depends on the pH, for pH 7 the bandgap around 3 eV. The hexagonal in micro size from the SEM image indicated that the carbon-lignin with ZnO nanoparticles attached at the surface. The degradation performance was increase with increasing the calcination temperature and pH 4 shows the lowest degradation ability. The best parameter of composite carbon-lignin/ZnO nanocrystalline ball-like hexagonal structure to reach 96.272% degradation performance are pH 7, 600 °C calcination temperature, and 90 min irradiation time.

**Keywords** Composite carbon-lignin/zinc oxide · *Jatropha curcas* L · Calcination temperature · pH · Degradation performance

## 1 Introduction

The textile industry is a company that harms the earth, specifically in the environment such as a river, lake, and sea. The untreated liquid waste which was then released into the natural environment that has environmental problems. Environmental problems around the world related to the textile industry are usually of water pollution due to the disposal of untreated waste and the use of toxic chemicals, especially during the processing stage. The waste is a critical

environmental concern, drastically reducing oxygen concentration affected to the presence of hydrosulfide which prevents light into the surface of water consequently damage of the aquatic ecosystem and causes of a large amount of environmental degradation and human disease, around 40% dyes used globally contain organically bound chlorine [1, 2].

Textile waste has high BOD (*Biological Oxygen Demand*) characteristics (from 700 to 2000 mg/l) and COD (*Chemical Oxygen Demand*) load, suspended solids, mineral oil, and residual dyes, 10–25% textile dyes are lost during the producing coloring, and 2–20% are directly disposed of liquid waste in different environmental components [3]. Recently conducted by Ref. [4, 5] multifunctional material based on Fe<sub>3</sub>O<sub>4</sub>-activated carbon (AC) composite of with a variety AC compositions was obtained, an ideal composition of 25% AC for absorbing liquid waste from the textile industry. The new problems of Fe as the basic material was considered to be a material that producing new waste by the oxidation processes that cause corrosion when it has been applied to the surrounding environment (natural). Ref. [6] evaluated the removal Cu<sup>2+</sup> and Zn<sup>2+</sup> in water utilizing the adsorption

✉ Dahlang Tahir  
dtahir@fmipa.unhas.ac.id

<sup>1</sup> Department of Environmental Management, Graduate Study Program, Hasanuddin University, 90245 Makassar, Indonesia

<sup>2</sup> Department of Physics, Hasanuddin University, 90245 Makassar, Indonesia

<sup>3</sup> Research Center for Physics, Indonesia Institute of Sciences, PUSPIPTEK, 15314 Jakarta, Tangerang Selatan, Indonesia

process using three bio-sorbents derived from castor biomass (bark, endosperm, endosperm + seed coat) and several studies conducted using AC [7–9] has been carried out but was still constrained by substantial funding and less environmentally friendly. Therefore, innovations with affordable and environmentally friendly concepts were needed as sustainable development goals (SDGs): point 6. Clean water and sanitation and point 7. affordable and clean energy [10–12].

For the present photocatalyst technology using the part of the plant, biomass has become a potential alternative technology to be developed. This method is believed to be very promising, especially cheap, has good adsorption ability, easily regenerated, and safety for the environment [13]. The innovation that became the idea in this study was to utilize biomaterials into environmental friendly as a bio-photocatalyst by using castor leaf (*Jatropha curcas L.*).

*Jatropha curcas L.* is a plant which resistant to drought, it able to grow fast in a barren and rocky field. Soil pH conditions suitable for this plant in between 5 and 6.5 [14]. Ref [15] reported that the castor leaf can grow in areas with an altitude of 0–800 m above the sea, and average temperatures between 25 and 35 °C. *Jatropha curcas L.* uses several components that were used as biodiesel producers such as seeds and stems, but the leaves have not been utilized.

The method used to reduce the negative effects of textile industry waste is treated by using chemical, physical, and biological methods. The combination of chemical and physical methods is used in the photocatalytic processes of liquid waste treatment. The photocatalyst is a method that can increase the rate of oxidation and reduction reactions induced by light. The use of photocatalysts is considered an efficient method of separating pollutant compounds by the absorbing visible radiation from the sunlight. Photocatalytic usually uses materials with the characteristics that are easily binding with other atoms of pollutants such as oxide materials, non-toxic, and also easy to synthesis [16–22]. The materials that fulfill these criteria are semiconductors [23–25]. The semiconductor

materials that have been used widely for photocatalytic applications in industrial wastes [25, 26] are ZnO, CuO, and Fe<sub>3</sub>O<sub>4</sub>. Furthermore, the potential of semiconductor material as a photocatalytic is due to an easily generated electron/hole (e<sup>-</sup>/h<sup>+</sup>) which can produce the radical atoms for the breakup waste bond and also this material can be doped with metal or non-metallic elements. The previous reported for semiconductor ZnO doped by various materials; graphene oxide [27], polyvinyl chloride (PVC) and PVA [28, 29], and carbon nanotube (CNT) [30] for photocatalyst and antibacterial applications.

In this research, the carbon-lignin/ zinc oxide hybrid composite nanocrystalline as photocatalyst materials mediated from an extract of castor leaf for various calcination temperature (500 °C, 550 °C, and 600 °C) and pH (4, 7, and 10). Structural properties, chemical bonding, and surface structure of bio-sorbent were analyzed by using powder x-ray diffraction (PXRD), Fourier transforms infra-red (FTIR), and scanning electron microscopy (SEM), respectively. For the application photocatalyst in the textile industry liquid waste analysis by calculating the degradation ability from the spectra of the UV-Vis spectrophotometer.

## 2 Materials and Method

### 2.1 Sample Preparation

In this study, the materials use to producing composite bio-sorbent is castor leaf (*Jatropha curcas L.*), Zinc acetate dihydrate (CH<sub>3</sub>COO)<sub>2</sub>Zn·2H<sub>2</sub>O (Merck), NaOH (Sodium Hydroxide) Merck, HCl (Hydrochloride acid) Merck, Aquades, and textile industry liquid waste. Castor leaf was cleaning by using distilled water, dried for 7 days at room temperature then crushed with a blender and then filtered to produce castor leaf powder. The castor leaf synthesis process can be seen in Fig. 1.

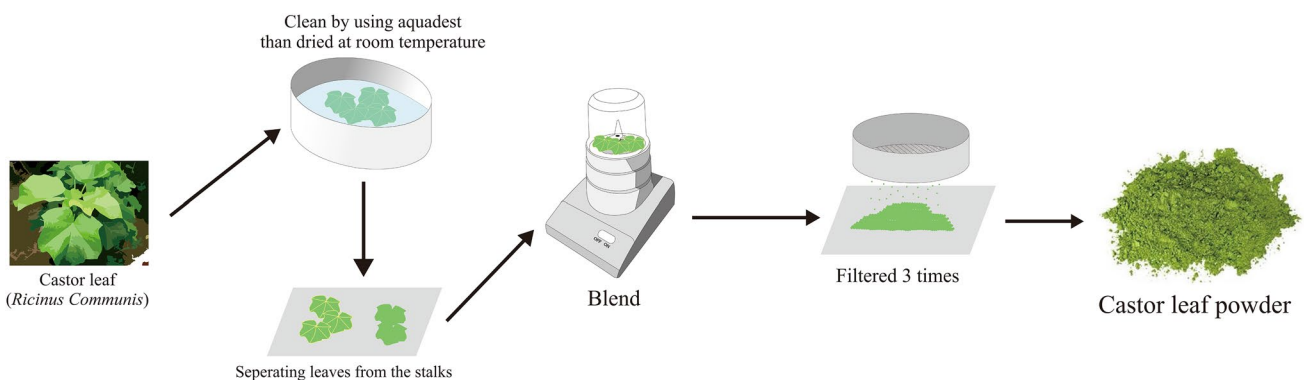


Fig. 1 Illustration process for synthesis of castor leaf powder

## 2.2 ZnO Crystallization Process

Fabrication of the castor leaf solution, castor leaf powder was dissolved with distilled water using a magnetic stirrer at 60 °C for 30 min. The Castor leaf solution was mixed with HCL / NaOH solution and zinc acetate solution to obtain the ZnO solution. After that, the ZnO solution centrifuged for 30 min at 12000 rpm to produce lignin/ZnO bonding together, and other compounds in solution will be separated and then heated using the microwave at 80 °C for 5 h. The calcination process was carried out at the temperature of 500 °C, 550 °C, and 600 °C for 2.5 h to get carbon-lignin/ZnO nanocrystalline. Illustration process in producing carbon-lignin/ZnO nanocrystalline can be seen in Fig. 2 a and the modification scheme as the effect of heating and calcination to form the hexagonal ball-like structure of carbon-lignin/ZnO material in Fig. 2b.

## 2.3 Photocatalytic Test

The absorption spectra were measured with a UV-Vis spectrometer. The percentage of methylene blue as a model textile industry waste degradation in the photo-catalyst process is calculated by the equation:  $D(\%) = \frac{C_0 - C_t}{C_0} \times 100\%$ , where  $D(\%)$  is the percentage of degradation,  $C_0$  is the initial absorbance (before irradiation), and  $C_t$  is the absorbance after time  $t$ .

## 2.4 Sample Characterization

Sample characterization is carried out by using powder X-ray diffraction (PXRD) ((Shimadzu 7000) with radiation  $\text{CuK}\alpha$  ( $\lambda = 1.5405 \text{ \AA}$ ) at range angle  $15^\circ \leq 2\theta \leq 80^\circ$  operation on 30 kV and 10 mA) for determine the structural properties of lignin/ZnO nanocrystal. Fourier Transform Infra-Red (FT-IR)

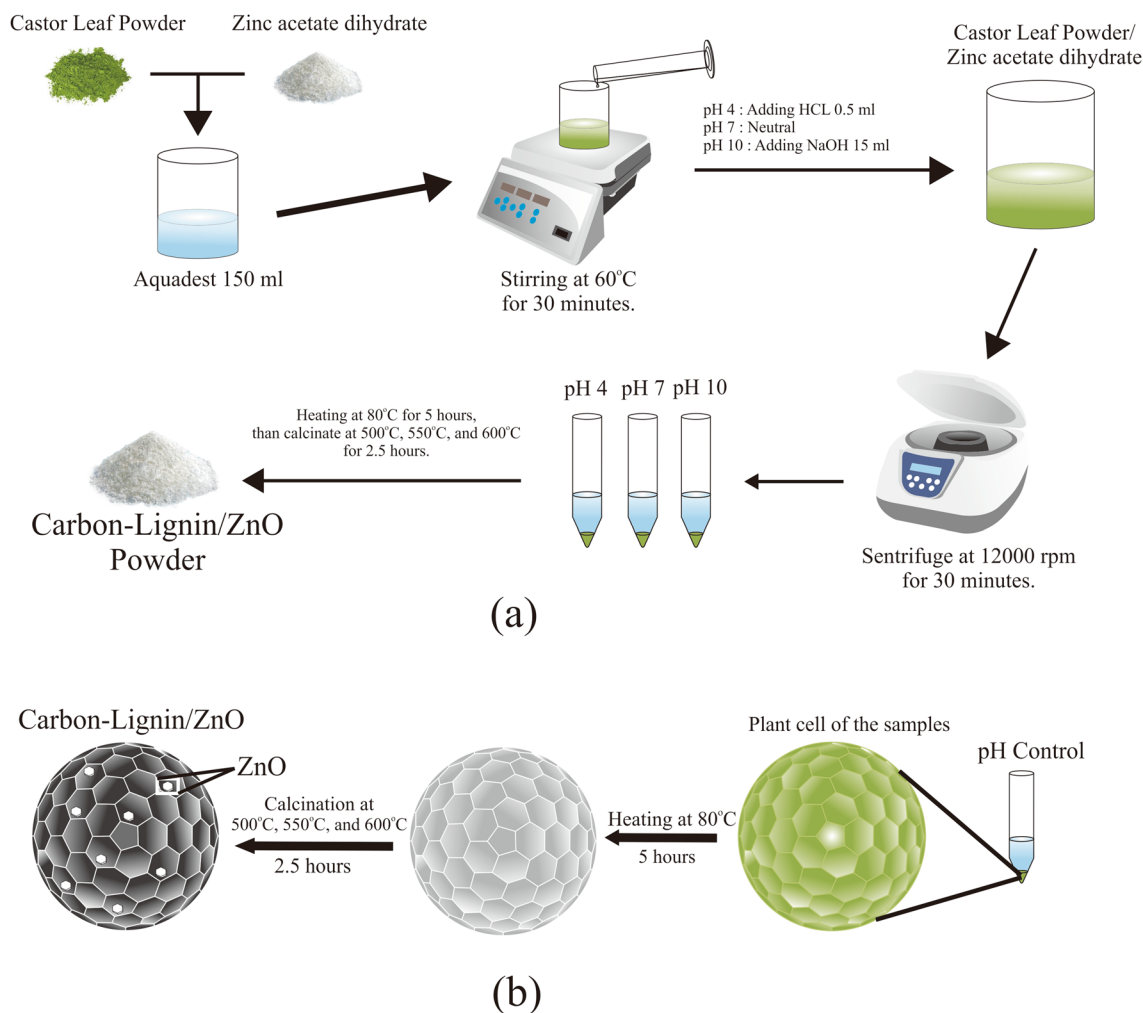


**Fig. 2** **a** Illustration process for producing carbon-lignin/ZnO nanopowder from castor leaf. **b** modification scheme as the effect of heating and calcination to form hexagonal structure of carbon-lignin/ZnO material

IRPrestige-21 FT-IR spectroscopy (Shimadzu Corp) to determine chemical bond and functional group of the samples for wavenumber 400–4000  $\text{cm}^{-1}$ , and UV-Vis spectroscopy (Shimadzu UV-Vis Spectrophotometer UV-1800) to determine the absorption of material at the wavelengths 400–800 nm in the range of visible light. The results of these measurements are used to analyze the absorption ability of composites to appropriate absorber for industrial liquid waste.

### 3 Analysis Data

#### 3.1 PXRD Spectra

The average crystallite size  $D$  determining from the Debye-Scherrer formula as follows [3–34]:

$$D = \frac{k\lambda}{B\cos\theta} \quad (1)$$

where,  $k$  is a constant (0.9),  $\lambda$  is an X-ray wavelength (for Cu is 0.154 nm),  $B$  is the full width at half the maximum (FWHM) of the diffraction peak, and  $\theta$  is the diffraction angle. The value of  $D$  used for the calculation of dislocation density ( $\delta$ ) by the relation  $\delta = 1/(D^2)$ .

The lattice parameter  $a$  and  $c$ , lattice volume ( $V$ ), and bond length ( $L$ ) are determined by the following equation:

$$\frac{1}{d^2} = \frac{4}{3} \frac{(h^2 + hk + k^2)}{a^2} + \frac{l^2}{c^2} \quad (2)$$

$$V = \frac{\sqrt{3}}{2} a^2 c \quad (3)$$

$$L = \sqrt{0.3a^2 + \left(\frac{1}{2} - u\right)^2 c^2} \text{ where } u = \frac{a^2}{3c^2} + 0.25 \quad (4)$$

Lattice parameter ( $a$  and  $c$ ), lattice volume ( $V$ ), and bond length ( $L$ ) based on the quantitative analysis of PXRD spectra. The porosity was calculated based on the Eq. (4–6) in Ref. [24], briefly repeated here by the following equation:

$$\rho_s = \frac{nM}{Nabc} = \frac{nM}{NV_{cal}} \quad (5)$$

$$\rho_{ex} = \frac{m}{V_{exp}} \quad (6)$$

$$P = \left(1 - \frac{\rho_{ex}}{\rho_s}\right) \times 100\% \quad (7)$$

where;  $\rho_s$  is the X-ray density,  $\rho_{ex}$  is the experimental density,  $P$  is the porosity ( $P$ )  $n$  is the number of molecules per unit cell,  $M$  is molecular weight,  $N$  is Avogadro number. The sample preparation for PXRD instrument is in the pellet form, it's easy to determine the mass ( $m$ ) and the volume ( $V_{exp}$ ). The crystallite size, lattice parameter, volume, porosity, bond length, porosity, and dislocation density are shown in Table 1.

#### 3.2 UV-Vis Spectra

There are two ways for determining the band gap with high accuracy, first, by quantitative analysis of reflection electron energy loss spectroscopy (REELS) spectra from the low loss region as reported in [35–39] and the second is by using quantitative analysis absorption spectra from the Uv-Vis spectroscopy as reported in [40]. In this study, we applied Tauc-plot relation by quantitative analysis of the Uv-Vis absorption spectra for determining the band gap and the value presented in Table 2. The Tauc-plot plot relation with  $\alpha$  is the absorption coefficient as follows:

**Table 1** Crystallite size, lattice parameter, and porosity derived from XRD spectra in Fig. 3 for carbon-lignin/ZnO nanoparticle at various calcination temperature (500 °C, 550 °C, and 600 °C) and various pH (4, 7 and 10)

Sample ID	Crystallite size (nm) (D)	Lattice parameter (Å)				Volume ( $V_{cal}$ )	Ratio (c/a)	Dislocation density ( $1/D^2$ ) ( $\text{nm}^{-2}$ )	Porosity (%)	Bond length (Å)
		a	Error	c	Error					
500-4	9.49	3.25047	0.00008	5.21684	0.00212	47.73429	1.60495	0.0111	93.70505	1.97930
500-7	9.29	3.26342	0.00065	5.23373	0.00186	48.27118	1.60376	0.0116	93.24108	1.98672
500-10	7.22	3.24980	0.00007	5.22578	0.00191	47.79638	1.60803	0.0192	93.40886	1.98011
550-4	14.47	3.26039	0.00026	5.22061	0.00071	48.06080	1.60122	0.0047	95.35249	1.98388
550-7	11.92	3.26801	0.00614	5.26187	0.01907	48.66733	1.61011	0.0070	95.00133	1.99203
550-10	7.22	3.26054	0.00070	5.23667	0.00206	48.21308	1.60607	0.0192	94.46662	1.98588
600-4	31.17	3.25846	0.00054	5.22017	0.00154	47.99987	1.60204	0.0010	96.93030	1.98026
600-7	11.93	3.26344	0.00041	5.22444	0.00112	48.18608	1.60090	0.0070	96.37334	1.98561
600-10	8.29	3.25738	0.00054	5.22341	0.00154	47.99783	1.60356	0.0146	96.36640	1.98297

$$\alpha = \frac{A(h\nu - E_g)^{1/2}}{h\nu} \quad (8)$$

where  $A$  is the coefficient of proportionality,  $h$  is the Planck constant,  $\nu$  is the frequency of light, and  $E_g$  is the band gap. The bandgap indicated by the cross point in the x-axis in

**Table 2** The rate constant ( $k_r$ ) and correlation coefficient values ( $R^2$ ) of carbon-lignin/ZnO synthesized from castor leaves for various calcination temperature and pH from degradation analysis in Fig. 10 and bandgap from quantitative analysis of UV-Vis spectra in Fig. 5

Sample	$k_r$	$R^2$	Bandgap
500-4	0.011	0.983	2.998
500-7	0.018	0.991	3.019
500-10	0.012	0.946	3.108
550-4	0.016	0.995	2.973
550-7	0.033	0.981	3.022
550-10	0.019	0.995	3.078
600-4	0.024	0.994	2.989
600-7	0.042	0.992	3.051
600-10	0.024	0.989	3.102

Fig. 6 (red line) from the quantitative analysis of UV-Vis absorption spectra.

## 4 Results and Discussion

Figure 3 a shows the X-ray diffraction pattern of carbon-lignin/ZnO nanocrystalline for pH.4, pH.7, and pH.10 with calcination temperature for each pH is 500 °C, 550 °C, and 600 °C. The diffraction patterns of carbon-lignin/ZnO nanocrystalline show at (110), (006), and (113) for various intensity. Diffraction peak (110) is a hexagonal crystal structure of ZnO [4]. The diffraction peak at below 30° and above 50° assigned by a vertical dashed line is contributed from carbon-lignin as reported in [41–43] and the small diffraction peak in between (110) and (006) assigned the contribution of the hydroxyl from the castor leaf sitting in the lattice of ZnO [42, 43]. Table 1 shows that when the calcination temperature increases the crystallite size and porosity was increase as can be seen for the same pH. For the lattice parameter ( $\text{\AA}$ ) the results look similar for all samples but for the dislocation density parameter, it will increase with increasing the calcination temperature and the pH. Spectrum XRD also shows that the higher calcination temperature and

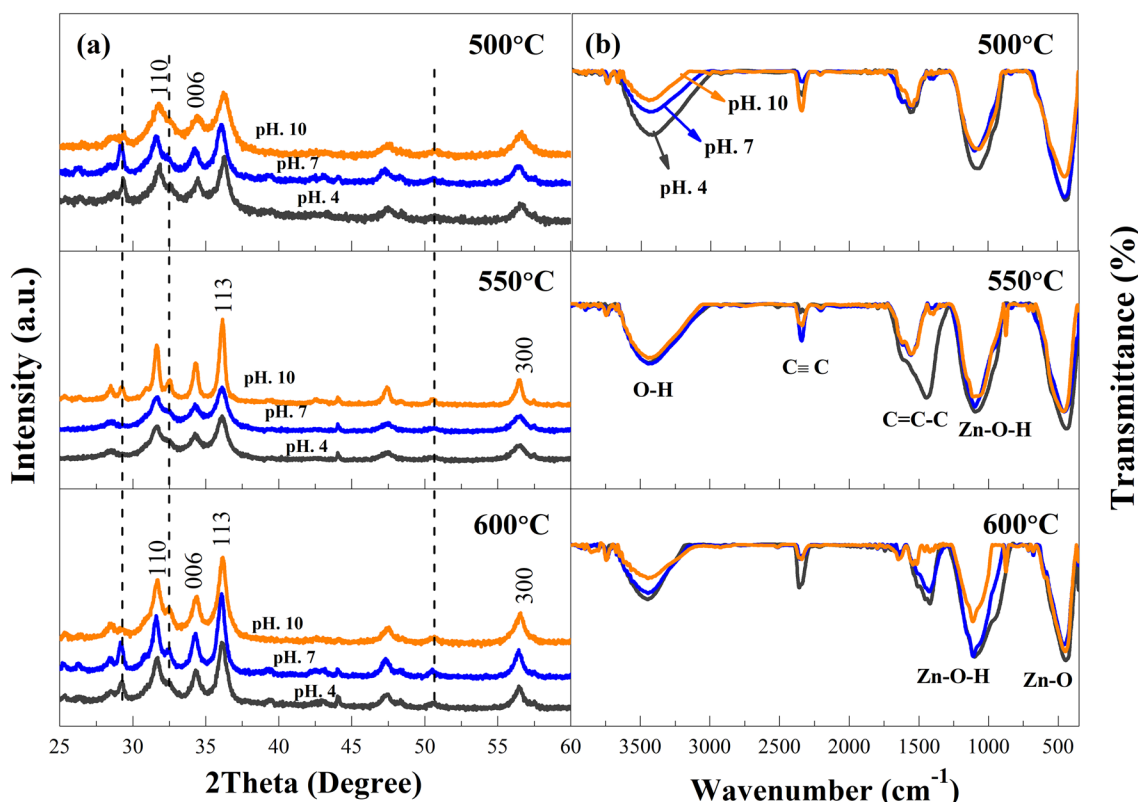


**Fig. 3** XRD spectra (a) and FTIR spectra (b) for carbon-lignin /ZnO nanopowder at various calcination temperature (500 °C, 550 °C, and 600 °C) and various pH (4, 7, and 10)



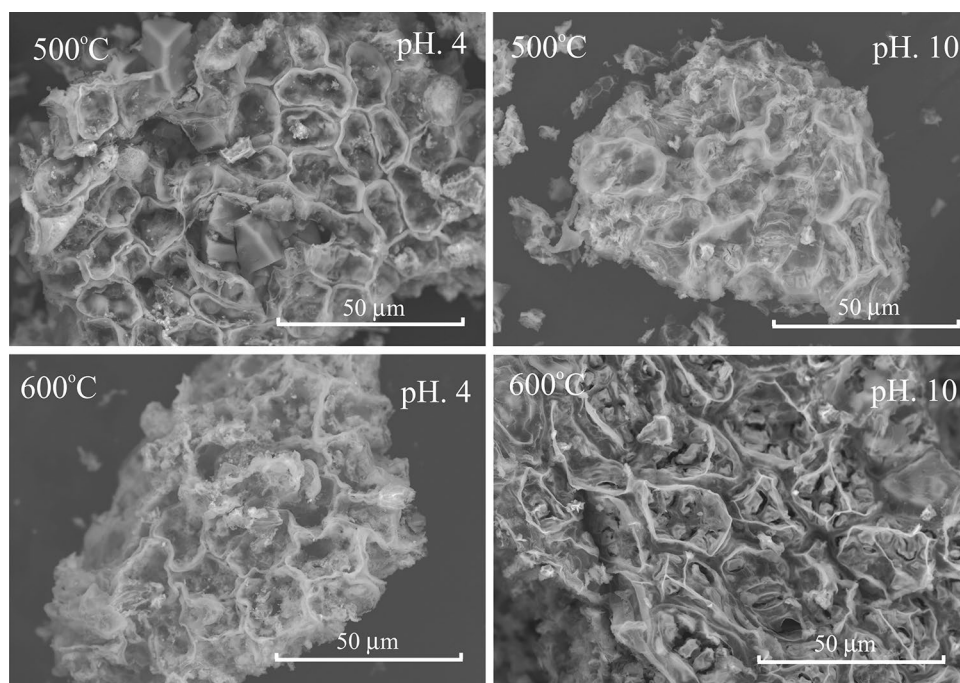
pH then the formation of the atom in the crystal structure is going to the stable position as shown in the peak diffraction at the calcination temperature 600 °C which is more stable as similarly reported in [23]. We can see in Table 1, the crystallite size for the same calcination temperature decreased with increasing the pH which is similarly reported in [25, 44, 45] that indicated the formation of atomic crystal in the lattice more stable. The crystallite size was increased with increasing the calcination temperature may due to the effect of solidification of atoms or probably the carbon atom sitting in the lattice of ZnO structure [42, 43, 46]. The crystallite size is strongly correlated with the level of the density and the volume of the atomic crystal in the material [4, 5, 16, 23, 32–34, 47]. Changes in the lattice ratio ( $c/a$ ) are proportional to the volume, porosity, bond length, and the dislocation density of carbon-lignin/ZnO nanocrystalline with calcination temperature and pH consequently as the effect of crystallite size [23, 45, 48].

Figure 3b shows the FTIR spectra of carbon-lignin/ZnO nanocrystalline for various: pH.4, pH.7, and pH.10 for each variation calcination temperature 500 °C, 550 °C, and 600 °C. The functional group of the O-H band at the wavenumber 3250–3750  $\text{cm}^{-1}$ . At the wavenumber 1250–1750  $\text{cm}^{-1}$ , there is a chemical bond in the form of C=C-C from the carbon-lignin, wavenumbers between 1000 and 1250  $\text{cm}^{-1}$  are formed in the form of Zn-O-H [42, 46, 49]. It is formed due to the bonding between Zn atoms with the OH molecule from carbon-lignin. For wavenumbers between 450 and 500  $\text{cm}^{-1}$  is formed chemical bond is Zn-O. FTIR spectrum also confirmed that the higher calcination temperature the peak of the O-H bond decreases, as we expected due to the

evaporation of the hydroxyl group in the composite. Also, there is a widening of the peak Zn-O-H bonds as increasing the calcination temperature, this is due to the Zn-O compound stretching the oxygen bond vibration from the carbon-lignin which is then occupied by O-H so that it becomes Zn-O-H as described by Ref. [44]. For the effect of pH, it can be seen that the highest intensity shown at a pH 7, which is supported by the peak of the Zn-O-H bond more stable than the other peaks. FTIR spectra also show compounds from the carbon-lignin by the presence of C≡C bonds at the wavenumbers from 2250 to 2350  $\text{cm}^{-1}$  as reported in Ref. [31, 49, 50]. Based on the analysis of FTIR spectra indicated that carbon-lignin/ZnO has been successfully synthesized from castor leaves as a natural material by the presence of C≡C, C=C-C, Zn-O, and Zn-OH bonds which is consistent with the XRD spectra.

Morphological analysis of carbon-lignin/ZnO synthesis from castor leaves is shown in Fig. 4. The results show that the particle shape of carbon-lignin/ZnO resembles a hexagonal ball-like shape with a magnification of each 50  $\mu\text{m}$  for each temperature and pH, which is dominated by white variations such as clouds and dark gray. The hexagonal shape in the micro size indicated that the carbon-lignin structure as reported in Ref. [42, 43, 46], the ZnO nanocrystalline probably attached in the surface of carbon-lignin which was consistent with the crystal structure from the PXRD spectra in Fig. 3a. The white color shown in the SEM surface morphology indicated the ZnO nanoparticle as reported by Ref. [51–53] and for the dark gray color assigned carbon-lignin from the leaf of the Castors. Based on the SEM surface image for the same magnification, 50  $\mu\text{m}$  shows for the

**Fig. 4** SEM image from the hexagonal structure of carbon-lignin/ZnO for calcination temperature 500 °C and 600 °C (pH 4 and 10)



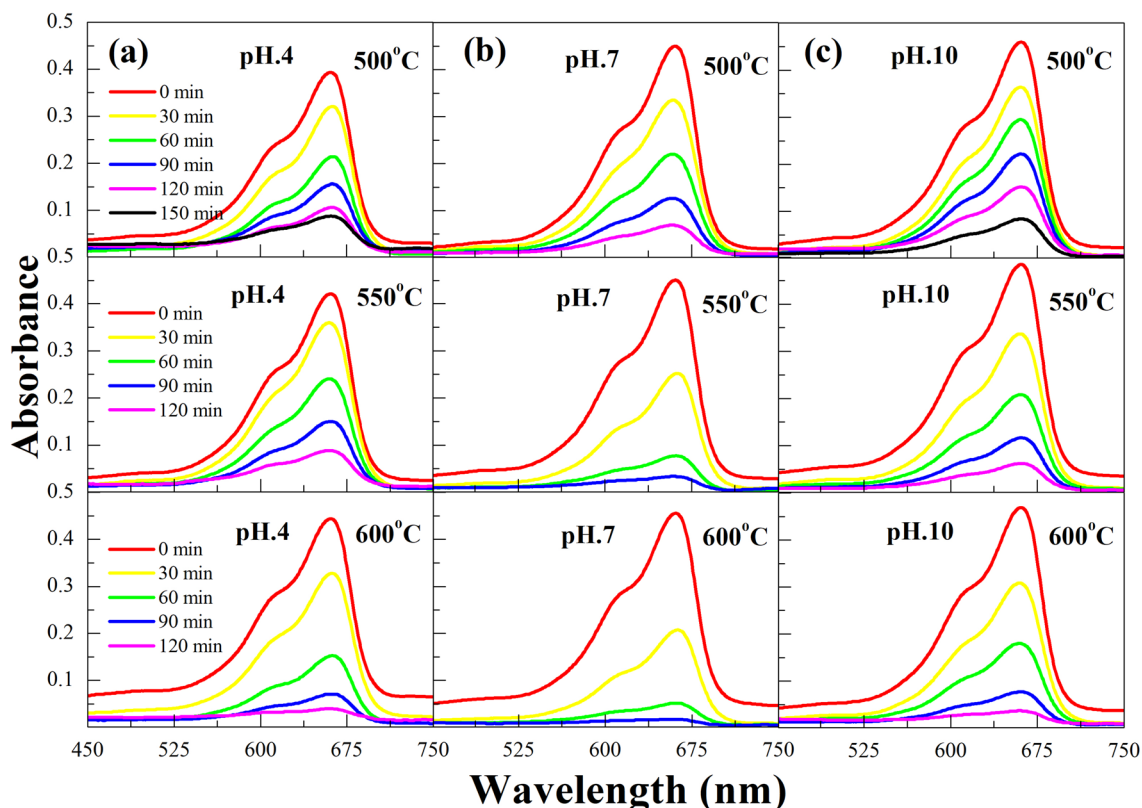
600 °C (pH 10) the morphological structure formed is also clearer, the bonding is better, and the surface structure which is supported by the lack of defects. The effect of temperature between 500 and 600 °C shows no significant different but for pH 4 at 600 °C shows destroy few part at the surface hexagonal structure as can be seen clearly in Fig. 4 (bottom left side).

Figure 5 shows Uv-vis spectra as a function of irradiation time for various calcination temperature and pH of the carbon-lignin/ZnO synthesized from castor leaves. The maximum absorbance peak at the wavenumbers in between 550  $\text{cm}^{-1}$  to 700  $\text{cm}^{-1}$  and the intensity of irradiation samples decreased with increasing the calcination temperature. For Uv-vis spectra at 0 min indicated non-irradiation was used for determining the bandgap by using the Tauc plot [40] as can be seen in Fig. 6.

The bandgap is the energy difference between the levels of conduction energy to the level of valence energy [35–39, 44] as can be seen in Fig. 6, the value of the bandgap indicated by the cross point between the line fits with the spectra to the x-axis. The bandgap is an important parameter for photocatalytic application due to the strongly related to the wavelength for generating pairs of electron and hole (e/h). The (e/h) is used to produce radical atoms or molecules,

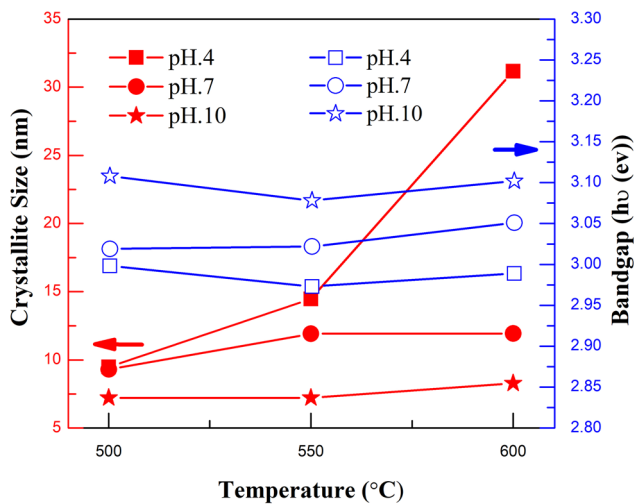
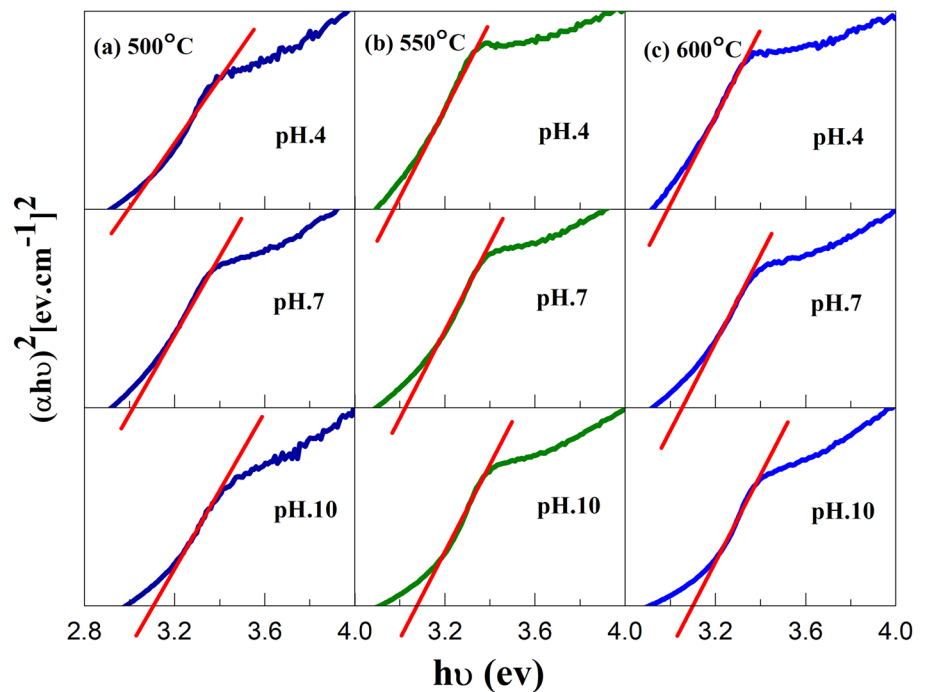
consequently, these radical going inside the molecule of harmful pollutants to break up the bonding until the final product is less harmful [54]. The bandgap strongly depends on the pH, for pH 4 the bandgap is less than 3 eV, for pH 7 the bandgap around 3 eV, and for pH 10 the bandgap is higher than 3 eV. The bandgap is in the range of visible region, similar reported from Ref. [55–57] analysis by photoluminescence spectra of nanocomposite ZnO/polyaniline [55] and ZnO nanorods [56, 57] for sensor applications. For more detail about bandgap value sees Table 2. At the calcination temperature is 550 °C the value of the bandgap is decreased probably due to the electronic structure as the effect of stretching of the O bond in ZnO [44]. This is also consistent with the FTIR spectra shows the widening peak of the Zn-O-H bond for the increasing the calcination temperature.

Figure 7 shows the relation between crystallite size and the bandgap of carbon-lignin/ZnO synthesized from castor leaves for various calcination temperatures and pH. It can be seen that the crystallite size small increase for pH 7 and 10 with increasing the calcination temperature, however for pH 4 remarkable increase for 600 °C indicated an unstable crystal structure. pH 7 and 10 are more stable for increasing the calcination temperature up to 600 °C [16, 23, 44, 45].



**Fig. 5** UV-visible absorption spectra of carbon-lignin/ZnO synthesized from castor leaves for various calcination temperature (500 °C, 550 °C, and 600 °C) and pH (4, 7, and 10)

**Fig. 6** Bandgap of carbon-lignin/ZnO synthesized from castor leaves for various calcination temperature (500 °C, 550 °C, and 600 °C) and pH (4, 7, and 10) determined from Figure by Tauch plot relation)



**Fig. 7** The relation between crystallite size and the bandgap of carbon-lignin/ZnO synthesized from castor leaves for various calcination temperature (500 °C, 550 °C, and 600 °C) and pH (4, 7, and 10)

pH 7 and 10 show small changes for the crystallite size and the bandgap for increasing the temperature up to 600 °C as shown in Fig. 7.

The results of the photocatalytic degradation of the blue methylene solution as a model textile industry waste are shown in Fig. 8 from the quantitative analysis of Uv-vis spectra in Fig. 5. The increase of the calcination

temperature then the degradation performance for each pH value is also increasing. For pH 7 at the calcination temperatures 500 °C, 550 °C, and 600 °C shows maximum degradation is 84.667%, 92.461%, and 96.272%, respectively. The maximum degradation yield was obtained at pH.7 at 550 and 600 °C which only takes 90 min irradiation to reach the maximum degradation while pH 4 and pH 10 requires irradiation up to 120 min. These results indicate that pH 7 can accelerate the degradation process [58], less for pH10, and small for pH 4 may due to the larger particle size [44].

Based on Fig. 9, the degradation rate constants ( $k_r$ ) and the correlation coefficient ( $R^2$ ) composite carbon-lignin/ZnO in this study are shown in Table 2. The rate constant increased with increasing the calcination temperature for the same pH. The best correlations are shown for pH 7 with a calcination temperature of 600 °C compared to the calcination temperature 500 and 550 °C. For pH 7 at 600 °C shows only 90 min irradiation to reach the highest rate constant and correlation coefficient. Based on these results it can be confirmed that the best parameter for the highest photocatalyst performance of carbon-lignin/ZnO synthesized from castor leaves is pH 7, bandgap around 3 eV, calcination temperature 600 °C, and the crystallite size around 12 Å. These parameters is the important parameter for supporting processes of high performance of photocatalyst by producing electron-hole pairs and avoid recombination subsequently produce the radical atoms which can break the structure of molecule textile industry waste [59].



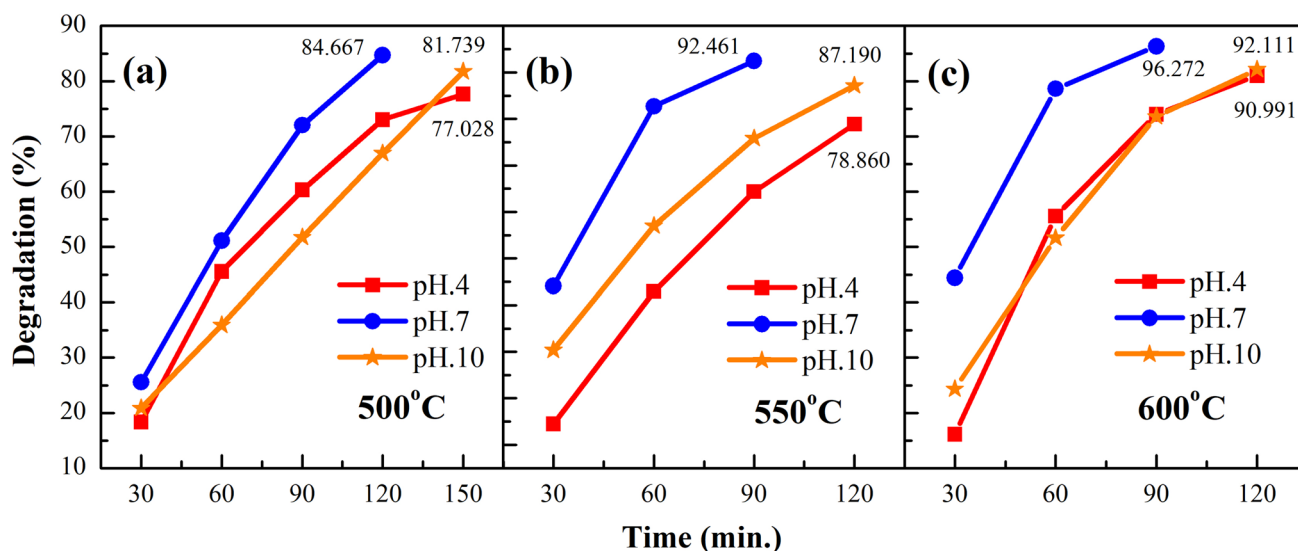
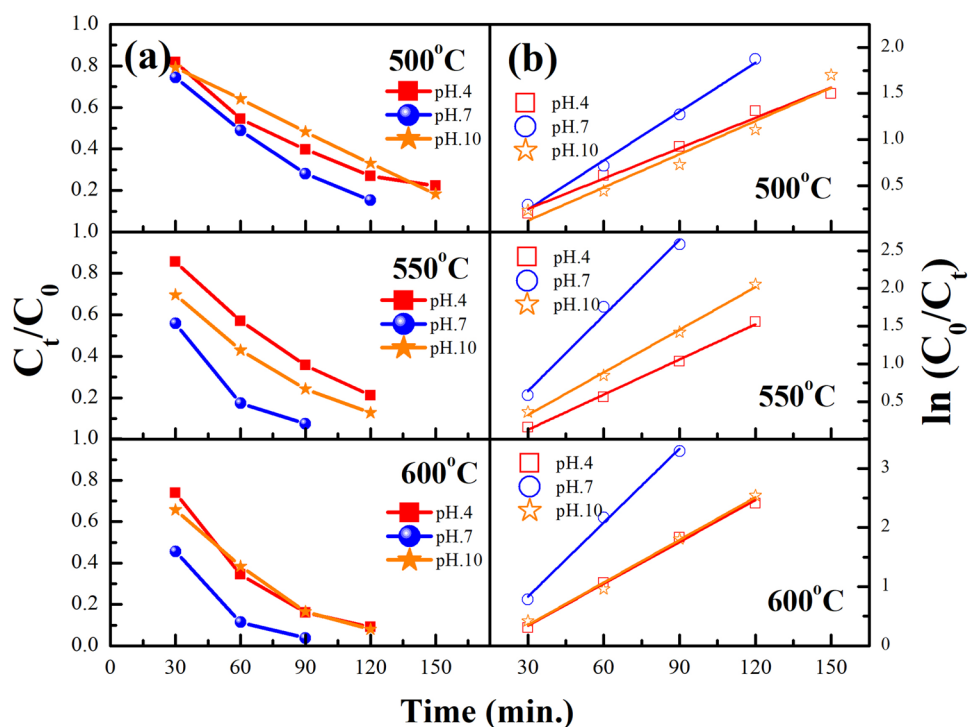


**Fig. 8** Percentage degradation of carbon-lignin/ZnO synthesized from castor leaves for various calcination temperature (500 °C, 550 °C, and 600 °C) and pH (4, 7, and 10)

**Fig. 9** Photocatalytic performance and kinetic curve of carbon-lignin/ZnO synthesized from castor leaves for various calcination temperature (500 °C, 550 °C, and 600 °C) and pH (4, 7, and 10)



## 5 Conclusion

In this research, composite carbon-lignin/ZnO successfully synthesized from *Jatropha curcas L* by various calcination temperatures (500 °C, 550 °C, and 600 °C) and pH (4, 7, and 10) for purifying of the textile industrial liquid waste. The diffraction peak at below 30° and above 50° assigned

from carbon-lignin and also diffraction peak in between (110) and (006) assigned of the hydroxyl from the castor leaf sitting in the lattice of ZnO. The crystallite size and the porosity were increases with increasing the calcination temperature for the same pH. Spectrum PXRD also shows that the higher calcination temperature and pH then the formation of the atom in the crystal structure is going to the stable position. FTIR spectra show compounds

from the carbon-lignin by the presence of  $C\equiv C$  bonds at the wavenumbers from 2250 to 2350  $\text{cm}^{-1}$ . Based on the analysis of FTIR spectra indicated that carbon-lignin/ZnO has been successfully synthesized from castor leaves as natural materials as evidenced by the presence of  $C\equiv C$ ,  $C=C-C$ , Zn-O bonds, and Zn-OH which is consistent with the PXRD spectra. Morphological analysis show hexagonal structure that the particle shape of carbon-lignin/ZnO with the ZnO nanoparticles attached in the wall of carbon-lignin. The degradation rate constants and the correlation coefficient of composite carbon-lignin/ZnO increase with increasing the calcination temperature for the same pH. In this study, confirmed that the best parameter for environmental friendly highest photocatalyst performance of carbon-lignin/ZnO synthesized from castor leaves is pH 7, bandgap around 3 eV, calcination temperature 600 °C, and the crystallite size around 12 Å.

**Acknowledgements** This work was supported by the PTM (Penelitian Tesis Magsiter): 1517/UN4.22?PT.01.03/2020 2020 funded by the Indonesian Government (Kemenristek/BRIN).

## References

1. K. Sana, A. Malik, Environmental and Health Effects of Textile Industry Wastewater, in *Environmental Deterioration and Human Health*, ed. by A. Malik, E. Grohmann, R. Akhtar (Springer, Dordrecht, 2014), pp. 55–71
2. A. Hoque, M. Mohiuddin, Z. Su, Effects of industrial operation on socio-environmental and public health degradation: evidence from a least developing country (LDC). *Sustainability* **10**(11), 3948 (2018)
3. A. Ashfaq, A. Khatoon, Waste management of textiles: A solution to environmental pollution. *International Journal of current microbiology and applied sciences* **3**(7), 780–787 (2014)
4. S. Ilyas, B. Abdullah, D. Tahir, Enhancement of absorbing frequency and photo-catalytic performance by temperature treatment of composites  $\text{Fe}_3\text{O}_4$ -AC nanoparticle, *Advanced Powder Technology*, (2020) (Article In Press)
5. D. Tahir, S. Ilyas, B. Abdullah, B. Armynah, H.J. Kang, Electronic properties of composite iron (II, III) oxide ( $\text{Fe}_3\text{O}_4$ ) carbonaceous absorber materials by electron spectroscopy. *Journal of Electron Spectroscopy and Related Phenomena* **229**, 47–51 (2018)
6. N.F. Cardoso, R.B. Pinto, E.C. Lima, T. Calvete, C.V. Amavisca, B. Royer, M.L. Cunha, T.H.M. Fernandes, I.S. Pinto, Removal of remazol black B textile dye from aqueous solution by adsorption. *Desalination* **269**(1–3), 92–103 (2011)
7. H. Treviño-Cordero, L.G. Juárez-Aguilar, D.I. Mendoza-Castillo, V. Hernández-Montoya, A. Bonilla-Petriciolet, M.A. Montes-Morán, Synthesis and adsorption properties of activated carbons from biomass of *Prunus domestica* and *Jacaranda mimosifolia* for the removal of heavy metals and dyes from water. *Ind. Crops Prod.* **42**, 315–323 (2013)
8. I.O. Saheed, F.A. Adekola, G.A. Olatunji, Sorption Study of Methylene Blue on Activated Carbon Prepared from *Jatropha curcas* and *Terminalia catappa* Seed Coats. *JOTCSA: Chemistry* **4**(1), 375–394 (2017)
9. H. Nacke, A.C. Goncalves Jr., M.A. Campagnolo, G.F. Coelho, D. Schwantes, M.G. dos Santos, D.L. Briesch, J. Jr, Zimmermann, Adsorption of Cu (II) and Zn (II) from water by *Jatropha curcas* L. as Biosorbent. *Open Chem.* **14**(1), 103–117 (2016)
10. J. Rosenthal, A. Quinn, A.P. Grieshop, A. Pillarisetti, R.I. Glass, Clean cooking and the SDGs: Integrated analytical approaches to guide energy interventions for health and environment goals. *Energy. Sustain. Dev.* **42**, 152–159 (2018)
11. B.M. Campbell, J. Hansen, J. Rioux, C.M. Stirling, S. Twomlow, E.L. Wollenberg, Urgent action to combat climate change and its impacts (SDG 13): transforming agriculture and food systems. *Current Opinion in Environmental Sustainability* **34**, 13–20 (2018)
12. N. Dilekli, I. Gazcarro, Testing the SDG targets on water and sanitation using the world trade model with a waste, wastewater, and recycling framework. *Ecol. Econ.* **165**, 106376 (2019)
13. B. Volesky, Biosorption and me. *Water Res.* **41**(18), 4017–4029 (2007)
14. G.D.P.S. Augustus, M. Jayabalan, G.J. Seiler, Evaluation and bioinduction of energy components of *Jatropha curcas*. *Biomass Bioenerg.* **23**(3), 161–164 (2002)
15. K. Wulchafo, W. Geja, Review Paper on Origin, Description, Distribution and Economic Importance of *Jatropha curcas*. *International journal of Current Research and Academic Review* **7**(6), 22–30 (2019)
16. S. Madhav, A. Ahamad, P. Singh, P.K. Mishra, A review of textile industry: Wet processing, environmental impacts, and effluent treatment methods. *Environ. Qual. Manage.* **27**(3), 31–41 (2018)
17. C. Maria Magdalane, K. Kaviyarasu, A. Raja, M.V. Arularasu, T. Genene, A.B. Mola, Isaev, Naif Abdullah Al-Dhabi, Mariadhas Valan Arasu, B. Jeyaraj, J. Kennedy, M. Maaza, Photocatalytic decomposition effect of erbium doped cerium oxide nanostructures driven by visible light irradiation: Investigation of cytotoxicity, antibacterial growth inhibition using catalyst. *J. Photochem. Photobiol., B* **185**, 275–282 (2018)
18. C. Maria Magdalane, K. Kaviyarasu, G. Maria Assuntha Priyadharsini, A.K.H. Bashir, N. Mayedwa Naif, A. Al-Dhabi, N. Matinise, M.V. Arasu, A.B. Isaev, S. Arokiyaraj, J. Kennedy, M. Maaza, Improved photocatalytic decomposition of aqueous Rhodamine-B by solar light illuminated hierarchical yttria nanosphere decorated ceria nanorods. *J. Mater. Res. Technol.* **8**(3), 2898–2909 (2019)
19. C. Maria Magdalane, K. Kaviyarasu, N. Matinise, N. Mayedwa, N. Mongwaketsi, D. Letsholathebe, G.T. Mola, Naif Abdullah Al-Dhabi, Mariadhas Valan Arasu, M. Heninic, J. Kennedy, M. Maaza, B. Jeyaraj, Evaluation on  $\text{La}_2\text{O}_3$  garlanded ceria heterostructured binary metal oxide nanoplates for UV/ visible light induced removal of organic dye from urban wastewater. *South African journal of chemical engineering* **26**, 49–60 (2018)
20. K. Kaviyarasu, C. Maria Magdalane, D. Jayakumar, Y. Samson, A.K. H. Bashir, M. Maaza, D. Letsholathebe, A.H. Mahmoud, J. Kennedy, High performance of pyrochlore like  $\text{Sm}_2\text{Ti}_2\text{O}_7$  heterojunction photocatalyst for efficient degradation of rhodamine-B dye with waste water under visible light irradiation. *Journal of King Saud University-Science* **32**(2), 1516–1522 (2020)
21. K. Kaviyarasu, C. Maria Magdalane, K. Kanimozhi, J. Kennedy, B. Siddhardha, E. Subba Reddy, N.K. Rotte, Chandra Shekhar Sharma, F.T. Thema, Douglas Letsholathebe, Genene Tessema Mola, M. Maaza, Elucidation of photocatalysis, photoluminescence and antibacterial studies of ZnO thin films by spin coating method. *Journal of Photochemistry and Photobiology B: Biology* **173**, 466–475 (2017)
22. K. Kasinathan, J. Kennedy, M. Elayaperumal, M. Henini, M. Maaza, Photodegradation of organic pollutants RhB dye using UV simulated sunlight on ceria based  $\text{TiO}_2$  nanomaterials for antibacterial applications. *Sci Rep* **6**, 38064 (2016)
23. B. Hendri, D. Abdullah, S. Tahir, Fatimah, New types composite copper (Cu) and activated carbon (C) for electromagnetic wave

- absorber materials. *Journal of Physics: Conference Series* **1242**, 012031 (2019)
24. D. Tahir, S. Ilyas, B. Abdullah, B. Armynah, K. Kim, H.J. Kang, Modification in electronic, structural, and magnetic properties based on composition of composites Copper (II) Oxide (CuO) and Carbonaceous material. *Materials Research Express* **6**, 035705 (2018)
  25. V. Muşat, M.B. Ibănescu, D. Tutunaru, F. Potecaşu, Fe-Doped ZnO Nanoparticles: Structural, Morphological, Antimicrobial and Photocatalytic Characterization. *Materials Science and Engineering* **1143**, 233–239 (2017)
  26. M. Mostafa, Waste water treatment in Textile Industries- the concept and current removal Waste water treatment in textile Industries - the concept and current removal technologies Mohammad Mostafa. *Journal of Biodiversity and Environmental Sciences* **7**(1), 501–525 (2016)
  27. T. Naseem, M. Zain-ul-Abdin, M. Waseem, S.U. Hafeez, S. Din, Haq, Mahfoz-ur-Rehman, Reduced Graphene Oxide/Zinc Oxide Nanocomposite: From Synthesis to its Application for Wastewater Purification and Antibacterial Activity. *J Inorg Organomet Polym* (2020)
  28. M. Guedri, B. Zaabat, A. Boudine, Hafdallah, Synthesis, Characterization, Structural, and Optical Properties of Polyvinyl Chloride/Zinc Oxide Nanocomposite Films for Photocatalysis Application. *J Inorg Organomet Polym* (2020)
  29. J.P. Prociak, K. Pszczółka, J. Chwastowski, P. Staron, A. Staron, E. Sikora, S. Mchalowski, M. Banach, Preparation of PVA-Based Composites with the Addition of Zinc Oxide Nanoparticles. *J Inorg Organomet Polym* **29**, 390–401 (2019)
  30. P. Farazmand, M. Khanlary, S. Fehli, A.S. Elahi, M. Ghoranneviss, Synthesis of Carbon Nanotube and Zinc Oxide (CNT–ZnO) Nanocomposite. *J Inorg Organomet Polym* **25**, 942–947 (2015)
  31. S. Suryani, A.N. Heryanto, Rusdaeni, D. Fahri, Tahir, Quantitative analysis of diffraction and infra-red spectra of composite cement/BaSO<sub>4</sub>/Fe<sub>3</sub>O<sub>4</sub> for determining correlation between attenuation coefficient, structural and optical properties. *Ceram. Int.* **46**(11), 18601–18607 (2020)
  32. B. Heryanto, D. Abdullah, Tahir, Mahdalia, Quantitative analysis of X-ray diffraction spectra for determine structural properties and deformation energy of Al, Cu and Si. *J. Phys.: Conf. Ser.* **1317**, 012052 (2019)
  33. H. Heryanto, B. Abdullah, D. Tahir, Analysis of structural properties of X-ray diffraction for composite copper-activated carbon by modified Williamson Hall and size-strain plotting methods. *J. Phys.: Conf. Ser.* **1080**, 012007 (2018)
  34. B. Heryanto, D. Abdullah, Tahir, Determination of Binding Energy For Cu and Cu<sub>2</sub>O Based X-Ray Diffraction Spectrum. *Journal of Physics: Conf. Ser.* **979**, 012055 (2018)
  35. D. Tahir, H. L. Kwon, H. C. Shin, S. K. Oh, H. J. Kang, S. Heo, J. G. Chung, J. C. Lee, S. Tougaard, Electronic and optical properties of Al<sub>2</sub>O<sub>3</sub>/SiO<sub>2</sub> thin films grown on Si substrate, *Journal of Physics D: Applied Physics* **43**, 255301 (2010).
  36. D. Tahir, S. Tougaard, Electronic and optical properties of selected polymers studied by reflection electron energy loss spectroscopy. *J. Appl. Phys.* **111**, 054101 (2012)
  37. D. Tahir, S.K. Oh, H.J. Kang, S. Tougaard, Quantitative analysis of reflection electron energy loss spectra to determine electronic and optical properties of Fe-Ni alloy thin films. *Journal of Electron Spectroscopy and Related Phenomena* **206**, 6–11 (2016)
  38. S. Heo, D. Tahir, J.G. Chung, J. C. Lee, K.H. Kim, J. Lee, H.I. Lee, G. S. Park, S.K. Oh, H. J. Kang, P. Choi, B. D. Choi, Band Alignment Of Atomic Layer Deposited (HfZrO<sub>4</sub>)<sub>1-x</sub>(SiO<sub>2</sub>)<sub>x</sub> Gate Dielectrics On Si (100), *Appl. Phys. Lett.* **107**, 182101 (2015)
  39. S. Suryani, D. Heryanto, Tahir, Stopping powers and inelastic mean free path from quantitative analysis of experimental REELS spectra for electrons in Ti, Fe, Ni, and Pd. *Surf Interface Anal.* **52**, 16–22 (2020)
  40. J. Kennedy, P.P. Murmu, J. Leveueur, A. Markwitz, J. Futter, Controlling preferred orientation and electrical conductivity of zinc oxide thin films by post growth annealing treatment. *Appl. Surf. Sci.* **367**, 52–58 (2016)
  41. S. Zhang, Y. Cui, B. Wu, R. Song, H. Song, J. Zhou, X. Chen, J. Liua, L. Cao, Control of graphitization degree and defects of carbon blacks through ball-milling. *RSC Adv.* **4**, 505–509 (2014)
  42. H. Wang, X. Qiu, W. Liu, D. Yang, Facile preparation of well-combined lignin-based carbon/ZnO hybrid composite with excellent photocatalytic activity. *Appl. Surf. Sci.* **426**, 206–216 (2017)
  43. Z. Zheng, J. Wang, Y. Wei, X. Liu, F. Yu, J. Ji, Effect of La-Fe/Si-MCM-41 catalysts and CaO additive on catalytic cracking of soybean oil for biofuel with low aromatics. *J. Anal. Appl. Pyrol.* **143**, 104693 (2019)
  44. F. Adam, A. Himawan, M. Aswad, D. Tahir, Structural properties and bonding characteristic of magnesium (Mg) doped zinc oxide (ZnO). *Journal of Physics: Conference Series.* **1317**, 012051 (2019)
  45. P.K. Labhane, G.H. Sonawane, S.P. Patil, V.R. Huse, Influence of Mg doping on ZnO nanoparticles decorated on graphene oxide (GO) crumpled paper like sheet and its high photo catalytic performance under sunlight. *Journal of physics and chemistry of solids* **114**, 71–82 (2018)
  46. Q. Wei, X. Yang, G. Zhang, D. Wang, L. Zuin, D. Banham, L. Yang, S. Ye, Y. Wang, M. Mohamedi, S. Sun, An active and robust Si-Fe/N/C catalyst derived from waste reed for oxygen reduction. *Appl. Catal. B* **237**, 85–93 (2018)
  47. S. Ilyas, B. Heryanto, D. Abdullah, Tahir, X-ray diffraction analysis of nanocomposite Fe<sub>3</sub>O<sub>4</sub>/activated carbon by Williamson-Hall and size-strain plot methods. *Nano-Structures & Nano-Objects* **20**, 100396 (2019)
  48. P.K. Labhane, L.B. Patle, V.R. Huse, G.H. Sonawane, S.H. Sonawane, Synthesis of reduced graphene oxide sheets decorated by zinc oxide nanoparticles: Crystallographic, optical, morphological and photocatalytic study. *Chem. Phys. Lett.* **661**, 13–19 (2016)
  49. J. Coates, In: Meyers, R.A. (Ed.), *Interpretation of Infrared Spectra, A Practical Approach, Encyclopedia of Analytical Chemistry*. Copyrights John Wiley & Sons Ltd, 1–23 (2019) (Available at: <http://www3.uma.pt/jrodrigues/disciplinas/QINO-II/Teorica/IR.pdf>)
  50. Q. Zhang, P. Chen, M. Zhuo, F. Wang, Y. Su, T. Chen, K. Yao, Z. Cai, W. Lv, G. Liu, Degradation of Indometacine by Simulated Sunlight Activated CDs-Loaded BiPO<sub>4</sub> Photocatalyst: Roles of Oxidative Species. *Appl. Catal. B* **221**, 129–139 (2018)
  51. S. Shuang, Z. Zhang, The effect of annealing treatment and atom layer deposition to Au/Pt nanoparticles-decorated TiO<sub>2</sub> nanorods as photocatalysts. *Molecules* **23**(3), 525 (2018)
  52. L.T.T. Nguyen, L.T.H. Nguyen, A.T.T. Duong, B.D. Nguyen, N. Quang Hai, V.H. Chu, T.D. Nguyen, L.G. Bach, Preparation, characterization and photocatalytic activity of La-doped Zinc Oxide nanoparticles. *Materials* **12**(8), 1195 (2019)
  53. W.E. Mahmoud, Synthesis and optical properties of Ce-doped ZnO hexagonal nanoplatelets. *J. Cryst. Growth* **312**(21), 3075–3079 (2010)
  54. Z. Xie, Y. Feng, F. Wang, D. Chen, Q. Zhang, Y. Zeng, W. Lv, G. Liu, Construction of carbon dots modified MoO<sub>3</sub>/g-C<sub>3</sub>N<sub>4</sub> Z-scheme photocatalyst with enhanced visible-light photocatalytic activity for the degradation of tetracycline. *Applied Catalysis B: Environmental* **229**, 96–104 (2018)
  55. M. Turemis, D. Zappi, M.T. Giardi, G. Basile, A. Ramanaviciene, A. Kapralovs, A. Ramanavicius, R. Viter, ZnO/Polyaniline Composite Based Photoluminescence Sensor for the Determination of Acetic Acid Vapor. *Talanta* **211**, 120658 (2020)

56. G.R. Tereshchenko, I. Yazdi, V. Konup, V. Smyntyna, R. Khranovskyy, Ramanavicius Application of ZnO Nanorods Based Whispering Gallery Mode Resonator in Optical Immunosensors. *Colloids and Surfaces B-Biointerfaces* **191**, 110999 (2020) Yakimova<sup>c</sup>, A
57. R. Viter, M. Savchuk, N. Starodub, Z. Balevicius, S. Tumenas, A. Ramanaviciene, D. Jevdokimovs, D. Erts, I. Iatsunskyi, A. Ramanavicius, Photoluminescence Immunosensor Based on Bovine Leukemia Virus Proteins Immobilized on the ZnO Nanorods. *Sensors and Actuators B Chemical* **285**, 601–606 (2019)
58. M. Chandrasekhar, H. Nagabhushana, S.C. Sharma, K.H.S. Kumar, N. Dhananjaya, D.V. Sunitha, C. Shivakumara, B.M. Nagabhushana, Particle size, morphology and color tunable ZnO:Eu<sup>3+</sup> nanophosphors viaplant latex mediated green combustion synthesis. *J. Alloys Compd.* **584**, 417–424 (2014)
59. R. Anugrahwidya, N. Yudasari, D. Tahir, Optical and structural investigation of synthesis ZnO/Ag Nanoparticles prepared by laser ablation in liquid. *Mater. Sci. Semiconduct. Process.* **105**, 104712 (2020)

**Publisher's Note** Springer Nature remains neutral with regard to jurisdictional claims in published maps and institutional affiliations.